Journal of Alloys and Compounds 511 (2012) 163–168

Contents lists available at SciVerse ScienceDirect

Journal of Alloys and Compounds

journal homepage: www.elsevier.com/locate/jallcom

Preparation of $Ni_{0.5}Zn_{0.5}Fe_2O_4/SiO_2$ nanocomposites and their adsorption of bovine serum albumin

Ruijiang Liu[a,b], Xiangqian Shen[a,*], Chengtao Jiang[a], Fuzhan Song[a], Hongxia Li[b]

[a] School of Material Science and Engineering, Jiangsu University, Zhenjiang 212013, PR China
[b] School of Pharmacy, Jiangsu University, Zhenjiang 212013, PR China

ARTICLE INFO

Article history:
Received 12 July 2011
Received in revised form 7 September 2011
Accepted 10 September 2011
Available online 16 September 2011

Keywords:
Ni–Zn ferrite
Citrate-gel
Porous silica layer
Grain size
Specific surface area
Adsorption
Bovine serum albumin
Protein

ABSTRACT

The magnetic nanocomposites of $(1-x)Ni_{0.5}Zn_{0.5}Fe_2O_4/xSiO_2$ (x = 0–0.2) were synthesized by the citrate-gel process and their absorption behavior of bovine serum albumin (BSA) was investigated by UV spectroscopy at room temperature. The gel precursor and resultant nanocomposites were characterized by FTIR, XRD, TEM and BET techniques. The results show that the single ferrite phase of $Ni_{0.5}Zn_{0.5}Fe_2O_4$ is formed at 400 °C, with high saturation magnetization and small coercivity. A porous, amorphous silica layer is located at the ferrite nanograin boundaries, with the silica content increasing from 0 to 0.20, the average grain size of $Ni_{0.5}Zn_{0.5}Fe_2O_4$ calcined at 400 °C reduced from about 18–8 nm. Consequently, the specific surface area of the nanocomposites ascends clearly with the increase of silica content, which is largely contributed by the increase in the thickness of the porous silica layer. The $Ni_{0.5}Zn_{0.5}Fe_2O_4/SiO_2$ nanocomposites demonstrate a better adsorption capability than the bare $Ni_{0.5}Zn_{0.5}Fe_2O_4$ nanoparticles for BSA. With the increase of the silica content from 0 to 0.05 and the specific surface area from about 49–57 m^2/g, the BSA adsorption capability of the $Ni_{0.5}Zn_{0.5}Fe_2O_4/SiO_2$ nanocomposites calcined at 400 °C improve dramatically from 22 to 49 mg/g. However, with a further increase of the silica content from 0.05 to 0.2, the specific surface area increase from about 57–120 m^2/g, the BSA adsorption for the nanocomposites remains around 49 mg/g, owing to the pores in the porous silica layer which are too small to let the BSA protein molecules in.

1. Introduction

Magnetic nanoparticles (MNPs) have attracted interests based on their fascinating superparamagnetic behavior, high saturation magnetization and relaxation [1,2]. Now, the MNPs have been widely applied to biological and medical areas [3–5], such as drug and gene delivery [6,7], the control of cells and cellular function [8,9], therapeutic hyperthermia [10,11], bioseparation [12,13], magnetic resonance imaging [14–17], and quantitative immunoassay [18,19]. Beyond the biomedical area, interesting studies have been reported on the use of MNPs for ferrofluids, data storage, and catalysis [20]. Recently, some magnetic nanoparticles, such as CoPt $Co_{1-x}Zn_xFe_2O_4/SiO_2$ $MnFe_2O_4$, CoCrMo [21–24], etc., have been reported for biomedical applications.

Ni–Zn ferrites are one of the most versatile magnetic materials as they have high saturation magnetization, high Curie temperature, chemical stability, low coercivity and biodegradability [25]. Many researchers have studied the synthesis of Ni–Zn ferrites [1,26–29]. However, for bio-related applications, pure Ni–Zn ferrite nanoparticles usually lead to problems associated with the formation of large aggregates, the alteration of magnetic properties, and their toxicity in the biological systems. The layer of protective coating offers magnetic particles an opportunity both to maintain their chemical stability and to reduce the potential toxicity without making an obvious impact on their magnetic properties.

Silica has been considered to be one of the most ideal coating layers of coating for MNPs due to its characteristic including high chemical stability, biocompatibility, and easy functionalization, which make it suitable for conjugation with proteins and *in vivo* applications [13,30–32].

Many efforts have been made on the design and synthesis of silica-coated magnetic nanoparticles (SMNPs) over the past few decades [33,34]. As we know, size and composition may influence the property and application of magnetic nanoparticles in biology and medicine, thus the controllable synthesis of well-defined silica-coated magnetic nanoparticles is crucial to the investigation of their magnetic properties and potential applications in biomedical sciences.

Bovine serum albumin (BSA) is the first biomolecule that has been used in biomedical applications, because it is a relatively large biomolecule and usually has a tendency to accumulate at the interface of solid surfaces [23,35,36], and its adsorption on

* Corresponding author. Tel.: +86 511 88791964; fax: +86 511 88791964.
E-mail address: shenxq@ujs.edu.cn (X. Shen).

0925-8388/$ – see front matter © 2011 Elsevier B.V. All rights reserved.
doi:10.1016/j.jallcom.2011.09.020

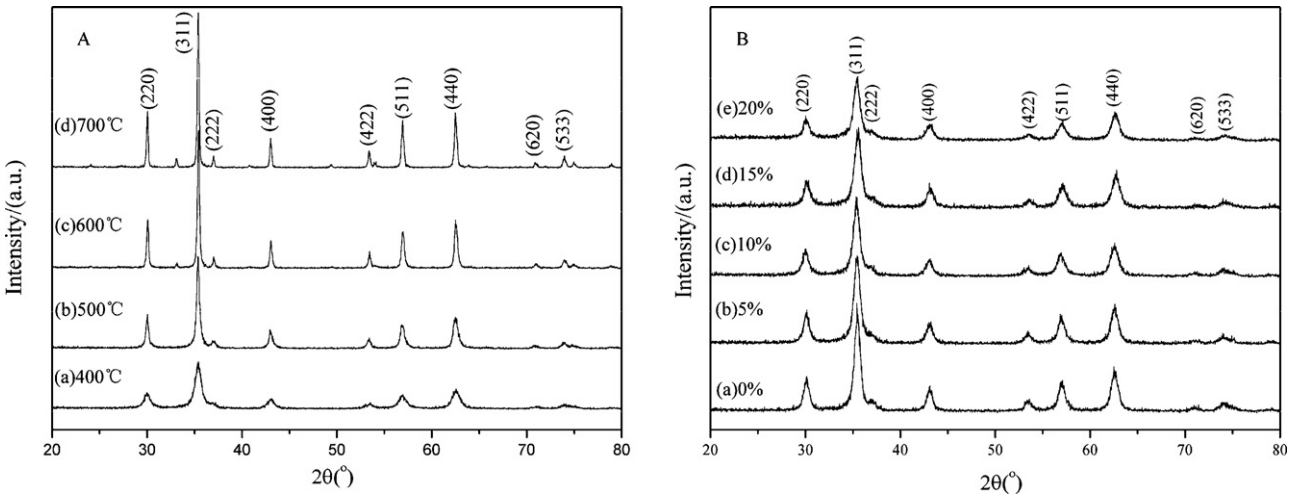

Fig. 1. XRD patterns of $(1-x)Ni_{0.5}Zn_{0.5}Fe_2O_4/xSiO_2$ nanocomposites with (A) silica content (x) of 0.10 calcined at various temperatures; (B) silica content (x) from 0 to 0.20 calcined at 400 °C.

surface of the $Ni_{0.5}Zn_{0.5}Fe_2O_4/SiO_2$ composite nanoparticles can act as adsorption models for other biomacromolecules. In this work, the magnetic $Ni_{0.5}Zn_{0.5}Fe_2O_4/SiO_2$ nanocomposites were synthesized via the citrate-gel process, and effects of silica content on the grain size, specific surface area and adsorption performance of bovine serum albumin on the $Ni_{0.5}Zn_{0.5}Fe_2O_4/SiO_2$ nanocomposites were investigated.

2. Experimental

The $(1-x)$ $Ni_{0.5}Zn_{0.5}Fe_2O_4/xSiO_2$ (x = 0–0.2, in weight ratio) nanocomposites were prepared via the citrate-gel process, which was described in detail for the mono-dispersed Ni–Zn ferrite nanopartices in our previous paper [37]. With reagent grade $Ni(NO_3)_2{\cdot}6H_2O$, $Zn(NO_3)_2{\cdot}6H_2O$ and $Fe(NO_3)_3{\cdot}9H_2O$, one mole of citric acid for one mole of metal and tetraethyl orthosilicate (TEOS) according to the various weight ratios of silica in $(1-x)Ni_{0.5}Zn_{0.5}Fe_2O_4/xSiO_2$ from x = 0 to 0.20 were mixed together in a beaker, and were dissolved in 100 ml distilled water. The mixed solution was magnetically stirred for 20–24 h at room temperature and the surplus water was removed in a vacuum rotary evaporator at 60–80 °C until a viscous liquid was obtained. Then, the viscous liquid was dried at 80 °C in an oven to obtain the dried gel precursor, which was calcined at various temperatures from 400 to 700 °C for 2 h in air to form loose nanocomposites.

The structures, compositions and morphologies of the gel precursors and the nanocomposites obtained were investigated by Fourier transform infrared spectroscopy (FTIR, Nexu670 spectrometer), X-ray diffraction (XRD, RIGAKU), transmission electron microscopy (TEM, JEM2100). The specific surface area and the pore size were measured by the Brunauere–Emmette–Teller (BET) method with the instrument of NOVA 2000e. The adsorption of BSA on the $Ni_{0.5}Zn_{0.5}Fe_2O_4/SiO_2$ nanocomposites was measured with a UV spectrophotometer (UV2550) at room temperature [37]. The adsorption capacity of BSA for the $Ni_{0.5}Zn_{0.5}Fe_2O_4/SiO_2$ nanocomposites can be calculated by the following equation [38]:

$$I = \frac{m_{BSA}(A_{BSA} - A_{mag})}{m_{mag}A_{BSA}}$$

where I refers to the adsorbed BSA amount of the $Ni_{0.5}Zn_{0.5}Fe_2O_4/SiO_2$ nanocomposites (mg/g), m_{BSA} is the total weight of BSA (mg), m_{mag} is the $Ni_{0.5}Zn_{0.5}Fe_2O_4/SiO_2$ nanocomposites weight (g), A_{BSA} is the UV absorbance value of blank BSA solution, and A_{mag} is the UV absorbance value of BSA solution after adsorption.

3. Results and discussion

3.1. Structural characterization of $Ni_{0.5}Zn_{0.5}Fe_2O_4/SiO_2$ nanocomposites

The X-ray diffraction (XRD) patterns of the $Ni_{0.5}Zn_{0.5}Fe_2O_4/SiO_2$ nanocomposites with silica weight content of 0.10 calcined at various temperatures for 2 h are shown in Fig. 1A. All the as-prepared nanocomposites show characteristic lines of Ni–Zn ferrite with a spinel structure, which indicates that single phase Ni–Zn ferrites are formed even at 400 °C (Fig. 1A(a)). It is well known that narrow lines width for XRD patterns indicate a high crystallinity and a larger grain size. Fig. 1A(a–d) shows that with an increase in the temperature, XRD peaks become sharper, suggesting that the crystallinity is higher and the particles size is larger at a higher temperature.

Fig. 1B shows the XRD patterns for the $Ni_{0.5}Zn_{0.5}Fe_2O_4/SiO_2$ nanocomposites with silica weight content from 0 to 0.20 calcined at 400 °C for 2 h. With the increase of silica weight content (Fig. 1B(a–d)), because of the non-crystalline nature of silica, the corresponding peaks become weaker and broader, which implies the crystallinity is lower and the particles size is smaller at a high silica content.

The average crystallite sizes of Ni–Zn ferrites can be calculated from the value of full-width (FWHM) at half-maximum of (3 1 1) plane using Scherrer's formula [39]:

$$D = \frac{0.89\lambda}{\beta \cos\theta}$$

where D is the crystallite size in nanometers, λ is the radiation wavelength (0.154056 nm for Cu Kα), β represents the bandwidth at half-intensity width of the relevant diffraction peak and θ is the corresponding diffraction peak angle. The results show that the grain sizes of nanocrystallites increase with the calcination temperature, while they descend from about 18 nm to 8 nm at 400 °C with the silica content increasing from 0 to 0.20. The reasons for this are that high temperature favors the atomic mobility and causes the grain growth, on the contrary, silica prevents the atomic mobility and causes the decrease of the grain size. The crystallite sizes show that the synthesized $Ni_{0.5}Zn_{0.5}Fe_2O_4$ is nano-crystallites. Therefore, the calcination temperature and the silica content are two important factors in controlling the synthesis of ferrite nanocrystallites.

Fig. 2 shows the TEM observations of the $Ni_{0.5}Zn_{0.5}Fe_2O_4/SiO_2$ composite nanoparticles with silica content of 0.20 calcined at 600 °C for 2 h. It can be estimated from Fig. 2 that the grain size of the $Ni_{0.5}Zn_{0.5}Fe_2O_4$ in nanocomposites is about 10–20 nm. These ferrite nanoparticles are well dispersed and the porous amorphous silica layer is located on the nanograin boundaries. The porous layer has very fine pores about 0.5–1.0 nm and is mesoporous [40]. This mesoporous amorphous silica layer will become thick with the silica content in the $Ni_{0.5}Zn_{0.5}Fe_2O_4/SiO_2$ nanocomposites, leading to a high specific surface area.

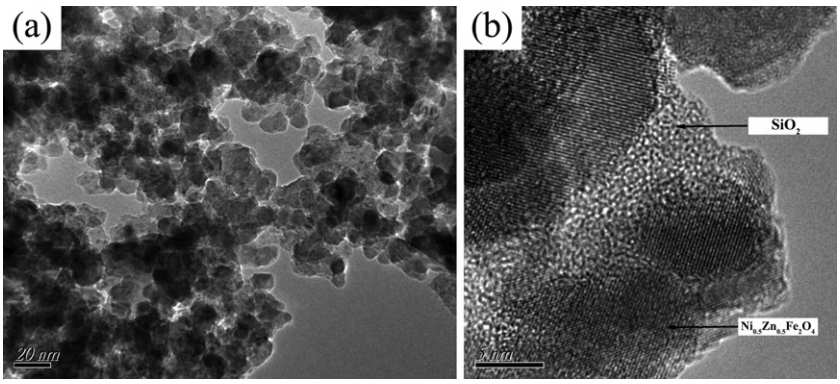

Fig. 2. HRTEM (a) and TEM (b) of $(1-x)Ni_{0.5}Zn_{0.5}Fe_2O_4/xSiO_2$ nanocomposites with silica content (x) of 0.20 calcined at 600 °C.

3.2. Magnetic properties

Fig. 3 shows the magnetic hysteresis loops of $(1-x)Ni_{0.5}Zn_{0.5}Fe_2O_4/xSiO_2$ nanocomposites calcined at 400 °C for 2 h with various silica contents. As showed in Fig. 3, all the samples have a narrow loop, which is indicative of a soft ferromagnetism nature. The saturation magnetization (M_s) values decrease from 77.3 Am^2/kg to 11.5 Am^2/kg with SiO_2 content (x) increasing from 0 to 0.2 or the crystalline size of the particles decreasing from 18 to 8 nm, as expected, since this parameter depends on the total mass of the magnetic phase ferrite. The lower value of M_s can be attributed to two reasons. First, the reduction of M_s is caused by the noncolinearity of magnetic moments at the nanoparticles surface, resulting in a decrease of the saturation magnetization for a higher SiO_2 content [41]. The non-magnetic SiO_2 can be considered as a magnetically dead layer at the surface, thus affecting the uniformity or the magnitude of magnetization due to quenching of surface moments. The surface effects reduce the saturation magnetization M_s with the decrease of the nanocrystallites' dimensions, which leads to a noncollinearity of magnetic moments on their surface [42]. Second, there are a lot of nonmagnetic SiO_2 and pores existing in the grain boundary as nonmagnetic gaps, which are not only the magnetic dilution but also a cut-off of the magnetic flux path in the nanocomposites. The ferrite nanoparticles are separated by the mesoporous SiO_2 layer and their interactions are reduced. These will result in smaller grain sizes and a lower value of M_s. Due largely to the soft ferromagnetism nature and nanograins of $Ni_{0.5}Zn_{0.5}Fe_2O_4$, there is almost no change in the small coercivity (Hc) of composite nanoparticles as the SiO_2 content increases or grain size decreases largely.

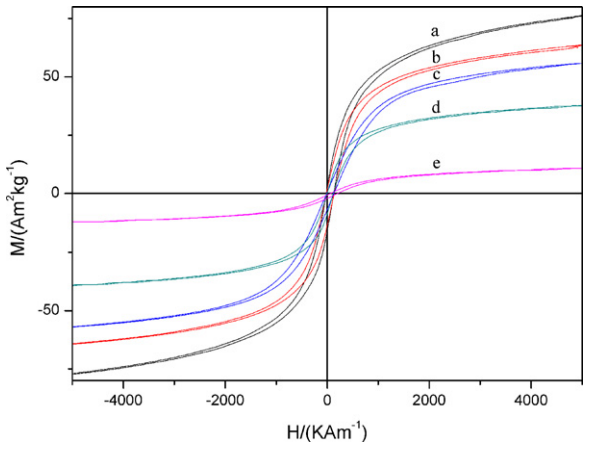

Fig. 3. Hysteresis loops of $(1-x)Ni_{0.5}Zn_{0.5}Fe_2O_4/xSiO_2$ nanocomposites calcined at 400 °C for 2 h with various silica contents (x=). (a) 0; (b) 0.05; (c) 0.1; (d) 0.15; (e) 0.2.

3.3. FTIR spectra of the gel precursor and $Ni_{0.5}Zn_{0.5}Fe_2O_4/SiO_2$ nanocomposites

Fig. 4 shows the FTIR spectra of the gel precursor and the as-prepared $Ni_{0.5}Zn_{0.5}Fe_2O_4/SiO_2$ nanocomposites in the range 400–4000 cm^{-1}. The gel precursor shows characteristic vibrations of silica and nitrate-citrates. Two broad bands at 3200–3700 and 1728 cm^{-1} are assigned to the O–H and H–O–H bending vibrations of citric acid and absorbed water [43], while the bands at 579 and 1384 cm^{-1} can be assigned to the asymmetrical NO_3^- stretching vibration that is directly related to the residual nitrate groups in the gel precursor [39]. The existence of the characteristic bands of NO_3^- indicates that the NO_3^- as a group exists in the structure of citrate gel during the gelation of the mixed solution formed from nitrates and citric acid. The bands at 890, 1439 and 1612 cm^{-1} are the characteristic peaks of the citrate where two peaks at 1439 and 1612 cm^{-1} correspond to the symmetrical and asymmetrical stretching vibrations of the carboxyl group, while the peak at 890 cm^{-1} is attributed to carbonyl group. The bands at 805 and 462 cm^{-1} characterize the silica network, as showed in Fig. 4a.

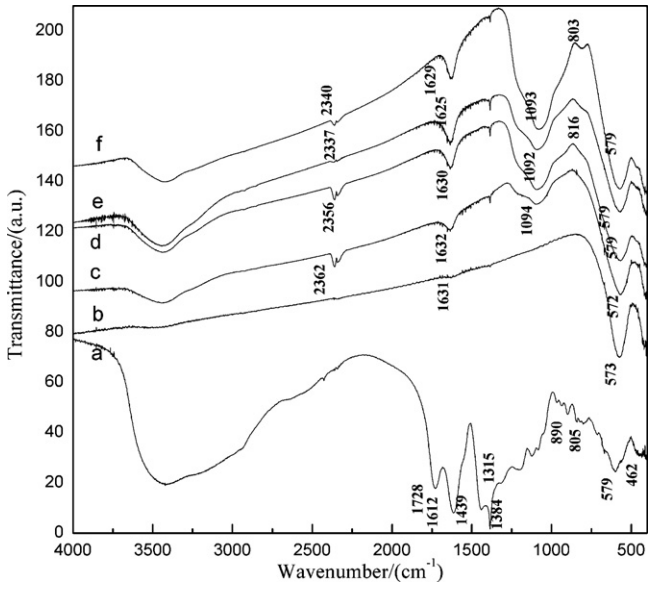

Fig. 4. FTIR spectra of the gel precursor (a) and the $(1-x)Ni_{0.5}Zn_{0.5}Fe_2O_4/xSiO_2$ nanocomposites calcined at 400 °C for 2 h with various silica contents (x=), (b) 0, (c) 0.05, (d) 0.10, (e) 0.15, (f) 0.20.

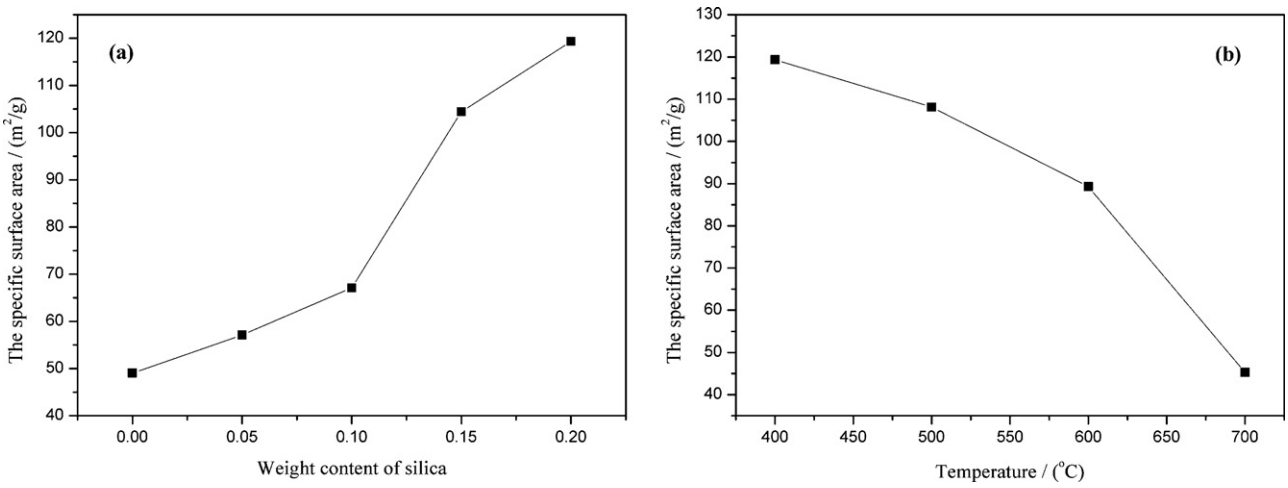

Fig. 5. The specific surface areas of $(1-x)Ni_{0.5}Zn_{0.5}Fe_2O_4/xSiO_2$ nanocomposites with (a) silica content (x) from 0 to 0.20 calcined at 400 °C, (b) silica content (x) of 0.20 at various temperatures from 400 °C to 700 °C.

Fig. 4b–f shows the IR spectra of the $Ni_{0.5}Zn_{0.5}Fe_2O_4/SiO_2$ nanocomposites with various silica contents calcined at temperature of 400 °C. Compared with Fig. 4a, the intensities of the broad bands associated with the absorbed water are drastically weakened. The peaks at 1728, 1612, 1439, 1384, 890, 840 and 579 cm^{-1} are disappeared. The new characteristic peak occurred in the region of 572–579 cm^{-1} can be assigned to the stretching mode of Fe–O at tetrahedral sites in the spinel structure, indicating that the spinel structure is basically formed at this temperature [44,45]. Furthermore, the ferrite-stretching band in Fig. 4b–f is shifted to higher wavenumbers and the intensity becomes weak with increasing silica content [46]. Meanwhile, it can be observed from Figs. 4c–f, with the silica content (x) increasing from 0.05 to 0.2, the characteristic peak at 2350–2370 cm^{-1} for Si–O bonds consequently becomes stronger and the silica layer thickness also increases.

3.4. Specific surface area of the $Ni_{0.5}Zn_{0.5}Fe_2O_4/SiO_2$ nanocomposites

The specific surface areas of the pure $Ni_{0.5}Zn_{0.5}Fe_2O_4$ and $Ni_{0.5}Zn_{0.5}Fe_2O_4/SiO_2$ nanocomposites were determined with the Brunauer–Emmett–Teller (BET) method, which involves the use of the BET equation [47].

$$\frac{1}{W}\cdot\frac{P}{P_0}=\frac{1}{W_mC}+\frac{C-1}{W_mC}\cdot\frac{P}{P_0}$$

In this equation, W is the weight of the gas adsorbed at a relative pressure P/P_0 and W_m is the weight of the adsorbate constituting a monolayer of the coverage, the term C is the BET constant.

Fig. 5a shows the specific surface areas of the $Ni_{0.5}Zn_{0.5}Fe_2O_4/SiO_2$ nanocomposites with various silica contents calcined at 400 °C, which indicates that the specific surface areas increase with the increase of silica content. When the silica content is 0.20, the specific surface area reaches 119.3 m^2/g. However, with the calcination temperature increasing from 400 °C to 700 °C, the specific surface areas of the $Ni_{0.5}Zn_{0.5}Fe_2O_4/SiO_2$ nanocomposites decrease, as showed in Fig. 5b. Therefore, in order to enhance the BSA adsorption for the $Ni_{0.5}Zn_{0.5}Fe_2O_4/SiO_2$ nanocomposites, it is advisable to calcine the $Ni_{0.5}Zn_{0.5}Fe_2O_4/SiO_2$ nanocomposites at 400 °C with silica content of 0.20. Meanwhile, they also have a high M_s value as showed in Fig. 3.

3.5. BSA adsorption of $Ni_{0.5}Zn_{0.5}Fe_2O_4/SiO_2$ nanocomposites

FTIR spectroscopy is a widely used technique to study protein conformation, and the different amide bond orientations within peptide backbone can be attributed to various secondary structures such as α-helix, β-sheets, β-turns and unordered structures [48]. The FTIR spectra of the bare $Ni_{0.5}Zn_{0.5}Fe_2O_4/SiO_2$ nanocomposites, $Ni_{0.5}Zn_{0.5}Fe_2O_4/SiO_2$ nanocomposites adsorbed BSA and pure BSA are shown in Fig. 6. In the FTIR spectrum of pure BSA (Fig. 6c), the peak at 3438 cm^{-1} is ascribed to the –OH vibration stretching, the amide A′ band is located at 3419 cm^{-1}, the broad bands at 1600–1700 cm^{-1} are assigned to the amide I region and the amide II region [38], and the bands at 1100–1200 cm^{-1} belong to C–O and C–N bond stretching [49]. Fig. 6a for the bare $Ni_{0.5}Zn_{0.5}Fe_2O_4/SiO_2$ nanocomposites actually is the same as Fig. 4f. While, the FTIR spectrum of the $Ni_{0.5}Zn_{0.5}Fe_2O_4/SiO_2$ nanocomposites adsorbed BSA (Fig. 6b) is characterized with a combination of characteristics in Fig. 6a and c. Compared with Fig. 6a, it is obvious that the characteristic peaks of BSA (the amide I region and the amide II region) occur in Fig. 6b, which indicates that BSA is adsorbed onto the $Ni_{0.5}Zn_{0.5}Fe_2O_4/SiO_2$ nanocomposites. In addition, as no new characteristic peaks are detected, the BSA protein does not bond to the $Ni_{0.5}Zn_{0.5}Fe_2O_4/SiO_2$ nanocomposites, and it is reasonably deduced

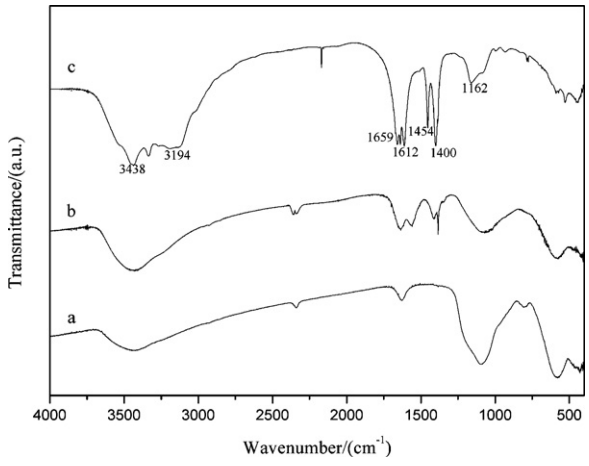

Fig. 6. FTIR spectra of (a) the pure $Ni_{0.5}Zn_{0.5}Fe_2O_4$ nanoparticles, (b) the $Ni_{0.5}Zn_{0.5}Fe_2O_4/SiO_2$ nanocomposites adsorbed BSA, (c) BSA.

Table 1
Effects of calcination temperature, grain size, specific surface area on BSA adsorption of bare $Ni_{0.5}Zn_{0.5}Fe_2O_4$ nanoparticles.

Calcination temperature (°C)	Grain size (nm)	Specific surface area (m^2/g)	BSA adsorption (mg/g)
400	14	49.0	22.0
500	24	59.6	33.9
600	33	39.9	10.5
700	45	18.8	7.8

that they are combined by the hydrogen bond and van der Waals force.

Table 1 shows the BSA adsorption of the pure $Ni_{0.5}Zn_{0.5}Fe_2O_4$ nanoparticles calcined at various temperatures from 400 °C to 700 °C with ferrite grain sizes. With the temperature increase, though the ferrite grain sizes ascend from 14 to 45 nm, the BSA adsorption is not clearly reduced, with a maximum value 33.9 mg/g for the pure $Ni_{0.5}Zn_{0.5}Fe_2O_4$ nanoparticles calcined at 500 °C with a grain size of 24 nm. Since bovine serum albumin are a globular protein with a prolate spheroid of dimensions of 4 nm × 4 nm × 14 nm [50], the possible reason for this phenomenon is that the $Ni_{0.5}Zn_{0.5}Fe_2O_4$ nanoparticles about 24 nm have a higher bio-affinity for BSA.

The BSA adsorptions for the $Ni_{0.5}Zn_{0.5}Fe_2O_4/SiO_2$ nanocomposites calcined at 400 °C with various silica contents are presented in Table 2. It can be seen that the $Ni_{0.5}Zn_{0.5}Fe_2O_4/SiO_2$ nanocomposites exhibit a much better adsorptivity for BSA compared with the pure $Ni_{0.5}Zn_{0.5}Fe_2O_4$ nanoparticles as represented in Table 1. With a very small amount of SiO_2 (x = 0.05) in the nanocomposites, the BSA adsorption is dramatically increased from 22.0 mg/g for the pure $Ni_{0.5}Zn_{0.5}Fe_2O_4$ nanoparticles to 49.2 mg/g. However, with the further increase of SiO_2 (x = 0.05–0.2) in the $(1-x)Ni_{0.5}Zn_{0.5}Fe_2O_4/xSiO_2$ nanocomposites, the BSA adsorptions tend to keep around 49 mg/g and are not obviously affected by the silica content when the nanocomposite contains a relatively high silica content. From the above FTIR analysis, the $Ni_{0.5}Zn_{0.5}Fe_2O_4/SiO_2$ nanocomposites absorbing of BSA is largely due to the hydrogen bond and van der Waals force, and thus it should be related to the specific surface area and Si–OH groups on the silica surface. However, referring to Fig. 6a and Table 2, the BSA adsorption of the $(1-x)Ni_{0.5}Zn_{0.5}Fe_2O_4/xSiO_2$ (x = 0.05–0.2) nanocomposites is basically not affected by the specific surface area which is clearly increased with the silica content. This phenomenon can be explained by the silica porous layer structure located at the boundaries of the $Ni_{0.5}Zn_{0.5}Fe_2O_4$ nanoparticles as showed in Fig. 2a and the calculated pore sizes as showed in Table 2. The silica porous layer with a very high specific surface area is yielded because of the TEOS decomposition, and this porous layer becomes thicker with the increase of silica content, which leads to a higher specific surface area for the nanocomposites. But the pores in the porous layer are too small to let the BSA in as it has a larger size of 4 nm × 4 nm × 14 nm [50]. Therefore, the measured BSA adsorption of the $(1-x)Ni_{0.5}Zn_{0.5}Fe_2O_4/xSiO_2$ (x = 0.05–0.2) nanocomposites is not related to the specific surface area and it will be enhanced by tailoring the pore size to suit entrance of BSA.

Table 2
Effects of silica content (x), specific surface area and average pore size on BSA adsorption of $(1-x)Ni_{0.5}Zn_{0.5}Fe_2O_4/xSiO_2$ nanocomposites calcined at 400 °C.

Silica content (x)	0	0.05	0.10	0.15	0.20
Specific surface area (m^2/g)	49.0	57.1	67.1	104.4	119.3
Average pore size (nm)	6.5	4.5	3.5	5.8	6.6
BAS adsorption (mg/g)	22.0	49.2	47.1	51.0	48.9

4. Conclusions

(1) The $(1-x)Ni_{0.5}Zn_{0.5}Fe_2O_4/xSiO_2$ (x = 0–0.2) nanocomposites have been successfully prepared by the facile citrate-gel process. The single phase of spinel $Ni_{0.5}Zn_{0.5}Fe_2O_4$ is formed at a low calcination temperature of 400 °C.

(2) The grain size of $Ni_{0.5}Zn_{0.5}Fe_2O_4$ in nanocomposites is largely influenced by the calcination temperature and silica content. With the calcination temperature increasing from 400 to 700 °C, the average ferrite grain size ascends, while it decreases with the silica content increasing from 0 to 0.20. Therefore, the $Ni_{0.5}Zn_{0.5}Fe_2O_4/SiO_2$ nanocomposite with SiO_2 content of 0.2 calcined at 400 °C is characterized with nanograins about 8 nm, a higher saturation magnetization and a smaller coercivity.

(3) The specific surface area of the $(1-x)Ni_{0.5}Zn_{0.5}Fe_2O_4/xSiO_2$ (x = 0–0.2) nanocomposites calcined at 400 °C increases with the increase of the silica content largely due to the formation of silica porous layer at the nanograins boundaries. It reaches 119.314 m^2/g when the silica content is 0.20.

(4) The $Ni_{0.5}Zn_{0.5}Fe_2O_4/SiO_2$ nanocomposites have an efficient adsorption of bovine serum albumin, with the BSA adsorption of about 49 mg/g, which is two times over the pure $Ni_{0.5}Zn_{0.5}Fe_2O_4$ nanoparticles.

(5) The BSA adsorption of the $Ni_{0.5}Zn_{0.5}Fe_2O_4/SiO_2$ nanocomposites is mainly caused by the hydrogen bond and van der Waals force. The adsorption capability is influenced by the specific surface area and the pore size for the nanocomposites. Although the specific surface area for the $Ni_{0.5}Zn_{0.5}Fe_2O_4/SiO_2$ nanocomposites increases obviously with the silica content increasing from 0.05 to 0.2, the BSA adsorption basically remains around 49 mg/g, which can be ascribed to the pore sizes, which are too smaller to let the larger protein molecules into the silica porous layer.

Acknowledgements

This work was financially supported by the National Natural Science Foundation of China (Grant No. 50134020) and the Jiangsu Province's Postgraduate Cultivation and Innovation Project (Grant No. CXZZ11_0557).

References

[1] G.P. Lopez, S.P. Silvetti, S.E. Urreta, A.C. Carreras, J. Alloys Compd. 505 (2010) 808–813.
[2] M. Gharagozlou, J. Alloys Compd. 495 (2010) 217–223.
[3] S. Laurent, S. Dutz, U.O. Hafeli, M. Mahmoudi, Adv. Colloid Interface. 166 (2011) 8–23.
[4] H.X. Peng, G.X. Liu, X.T. Dong, J.X. Wang, J. Xu, W.S. Yu, J. Alloys Compd. 509 (2011) 6930–6934.
[5] X.P. Shen, J.L. Wu, S. Bai, H. Zhou, J. Alloys Compd. 506 (2010) 136–140.
[6] M. Chorny, I. Fishbein, S. Forbes, I. Alferiev, Iubmb life. 63 (2011) 613–620.
[7] A.J. Cole, V.C. Yang, A.E. David, Trends Biotechnol. 29 (2011) 323–332.
[8] D. Sponarova, D. Horak, M. Trchova, P. Jendelova, V. Herynek, N. Mitina, A. Zaichenko, R. Stoika, P. Lesny, E. Sykova, J. Biomed. Nanotechnol. 7 (2011) 384–394.
[9] S.M.C. Berman, P. Walczak, J.W.M. Bulte, Wires Nanomed. Nanobi. 3 (2011) 343–355.
[10] J.H. Lee, J.T. Jang, J.S. Choi, S.H. Moon, S.H. Noh, J.W. Kim, J.G. Kim, I.S. Kim, K.I. Park, J. Cheon, Nat. Nanotechnol. 6 (2011) 418–422.
[11] R. Banerjee, Y. Katsenovich, L. Lagos, M. Mclintosh, X. Zhang, C.Z. Li, Curr. Med. Chem. 17 (2010) 3120–3141.
[12] M.X. Gao, C.H. Deng, X.M. Zhang, Expert Rev. Proteomic 8 (2011) 379–390.
[13] S. Kralj, M. Drofenik, D. Makovec, J. Nanopart. Res. 13 (2011) 2829–2841.
[14] F. Herranz, E. Almarza, I. Rodriguez, B. Salinas, Y. Rosell, M. Desco, J.W. Bulte, J. Ruiz-Cabello, Microsc. Res. Tech. 74 (2011) 577–591.
[15] E.K. Lim, Y.M. Huh, J. Yang, K. Lee, J.S. Suh, S. Haam, Adv. Mater. 23 (2011) 2436–2442.
[16] S.H. Yuk, K.S. Oh, S.H. Cho, B.S. Lee, S.Y. Kim, B.K. Kwak, K. Kim, I.C. Kwon, Biomacromolecules 12 (2011) 2335–2343.
[17] C.R. Shen, S.T. Wu, Z.T. Tsai, J.J. Wang, T.C. Yen, J.S. Tsai, M.F. Shih, C.L. Liu, Polym. Int. 60 (2011) 945–950.

[18] X.L. Zhao, Y.Q. Cai, F.C. Wu, Y.Y. Pan, H.Q. Liao, B.B. Xu, Microchem. J. 98 (2011) 207–214.
[19] J.K. Park, J. Jung, P. Subramaniam, B.P. Shah, C. Kim, J.K. Lee, J.H. Cho, C. Lee, K.B. Lee, Small 7 (2011) 1647–1652.
[20] F. Galeotti, F. Bertini, G. Scavia, A. Bolognesi, J. Colloid Interface Sci. 360 (2011) 540–547.
[21] Y.J. Zhang, Y.T. Yang, Y. Liu, Y.X. Wang, L.L. Yang, M.B. Wei, H.G. Fan, H.J. Zhai, X.Y. Liu, Y.Q. Liu, N.N. Yang, Y.H. Wu, J.H. Yang, J. Phys. D: Appl. Phys. 44 (2011) 295003.
[22] E. Girgis, M.M.S. Wahsh, A.G.M. Othman, L. Bandhu, K.V. Rao, Nanoscale Res. Lett. 6 (2011) 460.
[23] H.F. Liang, Z.C. Wang, Mater. Chem. Phys. 124 (2010) 964–969.
[24] C.V. Vidal, A.O. Juan, A.L. Munoz, Colloids Surf., B 80 (2010) 1–11.
[25] Q.A. Pankhurst, N.K.T. Thanh, S.K. Jones, J. Dobson, J. Phys. D: Appl. Phys. 42 (2009) 22401.
[26] G.S. Shahane, A. Kumar, M. Arora, R.P. Pant, K. Lal, J. Magn. Magn. Mater. 322 (2010) 1015–1019.
[27] S. Kumar, V. Singh, S. Aggarwal, U.K. Mandal, R.K. Kotnala, Mat. Sci. Eng. B-Solid 166 (2010) 76–82.
[28] B. Ghosh, S. Kumar, Hyperfine Interact 183 (2011) 163–169.
[29] A. Sutka, K.A. Gross, G. Mezinskis, G. Bebris, M. Knite, Phys. Scr. 83 (2011) 025601.
[30] A. Kathiravan, R. Renganathan, S. Anandan, Polyhedron 28 (2009) 157–161.
[31] B. Ori, J. Myoseon, B. David, P. Kevin, Inhal. Toxicol. 23 (2011) 532–543.
[32] Y.M. Yang, J.X. Aw, K. Chen, F. Liu, P. Padmanabhan, Y.L. Hou, Z. Cheng, B.G. Xing, Chem. Asian J. 6 (2011) 1381–1389.
[33] O. Kaman, P. Veverka, Z. Jirak, M. Marysko, K. Knizek, M. Veverka, P. Kaspar, M. Burian, V. Sepelak, E. Pollert, J. Nanopart. Res. 13 (2011) 1237–1252.
[34] T. Kim, E. Momin, J. Choi, K. Yuan, H. Zaidi, J. Kim, M. Park, N. Lee, M.T. McMahon, A. Quinones-Hinojosa, J.W.M. Bulte, T. Hyeon, A.A. Gilad, J. Am. Ceram. Soc. 133 (2011) 2955–2961.
[35] T. Kopac, K. Bozgeyik, J. Yener, Colloids Surf., A 322 (2008) 19–28.
[36] C.H. Zhu, H.B. Shen, R.Y. Xu, H.Y. Wang, J.M. Han, Acta Phys. Chim. Sin. 23 (2007) 1583–1588.
[37] C.T. Jiang, R.J. Liu, X.Q. Shen, L. Zhu, F.Z. Song, Powder Technol. 211 (2011) 90–94.
[38] B.F. Pan, F. Gao, H.C. Gu, J. Colloid Interface Sci. 284 (2005) 1–6.
[39] K.H. Wu, Y.M. Shin, C.C. Yang, G.P. Wang, D.N. Horngc, Mater. Lett. 60 (2006) 2707–2710.
[40] K. Katsuya, S. Makoto, T. Masaki, S. Takao, J. Ceram. Soc. Jpn. 118 (2010) 410–416.
[41] M. Ma, Y. Zhang, X.B. Li, D.G. Fu, H.Q. Zhang, N. Gu, Colloids Surf., A 224 (2003) 207–212.
[42] C. Caizer, Mat. Sci. Eng. B-Solid 100 (2003) 63–68.
[43] L.H. Shi, D.B. Li, B. Hou, Y.H. Sun, Chin. J. Catal. 28 (2007) 999–1002.
[44] W. Ponhan, S. Maensiri, Solid State Sci. 11 (2009) 479–484.
[45] Y.W. Ju, J.H. Park, H.R. Jung, Mat. Sci. Eng. B-Solid 147 (2008) 7–12.
[46] K.H. Wu, W.C. Huang, C.C. Yang, J.S. Hsu, Mater. Res. Bull. 40 (2005) 239–248.
[47] L.Y. Zhu, G. Yu, W.W. Qin, X.Q. Wang, D. Xu, J. Alloys Compd. 492 (2010) 456–460.
[48] H.D. Wang, C.H. Niu, Q.q. Yang, I. Badea, Nanotechnology 22 (2011) 1–11.
[49] J.F. Shen, M. Shi, B. Yan, H.W. Ma, N. Li, Y.Z. Hua, M.X. Ye, Colloids Surf., B 81 (2010) 434–438.
[50] S.J. McClellan, E.I. Franses, Colloids Surf., B 28 (2003) 63–75.